Proceedings of the 2020 Winter Simulation Conference
K.-H. Bae, B. Feng, S. Kim, S. Lazarova-Molnar, Z. Zheng, T. Roeder, and R. Thiesing, eds.

A NEURAL NETWORK FOR SENSOR HYBRIDIZATION IN ROCKET GUIDANCE

Raúl de Celis
Pablo Solano-López
Luis Cadarso

Aerospace Systems and Transport Research Group
European Institute for Aviation Training and Accreditation
Rey Juan Carlos University
Fuenlabrada
Madrid, 28943, SPAIN

ABSTRACT

Improving accuracy is cornerstone for ballistic rockets. Using inertial navigation systems and Global Navigation Satellite Systems (GNSS), accuracy becomes independent of range. However, during the terminal phase of flight, when movement is governed by non-linear and highly changing forces and moments, guidance strategies based on these systems provoke enormous errors in attitude and position determination. Employing additional sensors, which are independent of cumulative errors and jamming, such as the quadrant photo-detector semi-active laser, can mitigate these effects. This research presents a new non-linear hybridization algorithm to feed navigation and control systems, which is based on neural networks. The objective is to accurately predict the line of sight vector from multiple sensors measurements. Non-linear simulations based on real flight dynamics are used to train the neural networks. Simulation results demonstrate the performance of the presented approach in a 6-DOF simulation environment showing high accuracy and robustness against parameter uncertainty.

1 INTRODUCTION

Navigation signals from Global Navigation Satellite Systems (GNSS) are commonly used nowadays in aerospace applications. Unfortunately, reliability decreases inversely proportional to the requirement of the application for which it is designed. Note that attenuation and loss of the GNSS signal result in reduced signal / noise relationship. To lessen these effects and defend against jamming, independent sources of navigation information are needed.

Although Inertial Navigation Systems (INS), such as Inertial Measurement Units (IMUs) are independent of external perturbations, they present important deficiencies, such as inertial sensor (gyro and accelerometer) imperfections which are source of cumulative errors, incorrect navigation system initialization, and imperfections in the implemented gravity model. However, INS are excellent source of navigation information when combined with GNSS receivers, which can minimize errors in INS (de Celis, Cadarso, and Sánchez 2017).

Cost and precision have always been set as fundamental attributes of projectile performances. However, they are counter-posed objectives. Precision aims at minimizing "collateral damage". Low values for this damage can suppress the feasibility of military action. (Hamilton 1995). In order to reduce costs while maintaining an acceptable precision level, expensive inertial navigation systems can be replaced with less precise devices as long as the accessibility and persistence of the GNSS signal are guaranteed, to update the inertial system in order to limit the growth of errors. However, many scenarios feature high uncertainty. An approach to lower costs and collateral damage is to merge signals of several low-cost sensors, which

978-1-7281-9499-8/20/$31.00 ©2020 IEEE

enables improvement of overall accuracy. The benefits of integrated data fusion has been shown in many antisubmarine, strategic air, and land warfare applications (Waltz and Buede 1986). Data fusion algorithms for 6 degrees of freedom missiles are described in (Nguyen, Tyan, and Lee 2016). The advantages and issues in utilizing diverse sorts of INS expanded with GNSS updates have been considered by (Schmidt and Phillips 2011). In addition to INS/GNSS hybridization, a group of nonlinear observers are described by (Bryne, Hansen, Rogne, Sokolova, Fossen, and Johansen 2017). On the off chance that different sensors are accessible, they might be extra contributions to a filter, e.g., the Kalman filter (de Celis, Cadarso, and Sánchez 2017).

Similarly to (de Celis, Cadarso, and Sánchez 2017), the need to develop new Guidance, Navigation and Control (GNC) systems has motivated research on stability and controllability of these aerial platforms. Based on missile proportional navigation, (Zhao and Zhou 2015; Creagh and Mee 2010) presents cooperative strategies for multiple missiles based on the traditional Proportional Navigation (PN). An attitude control-system design for a spinning sounding rocket, which features a proportional, integral, and derivative (PID) type controller, is developed in (Lee, Sun, Tahk, and Lee 2001). Proportional-derivative navigation guidance laws for the terminal phase are proposed in (Lechevin and Rabbath 2012; Wang, Wang, and Gao 2015). The line of sight is reconstructed in (Nesline and Zarchan 1985). In (Zhang, Sun, and Chen 2012), a finite-time convergent sliding-mode guidance law with terminal impact angle constraint is presented. A complete design concerning the guidance and autopilot modules for a class of spin-stabilized fin-controlled projectiles is presented in (Theodoulis, Gassmann, Wernert, Dritsas, Kitsios, and Tzes 2013).

But even in GNSS/IMU integrated systems, there exist unknown disturbances and abnormal measurements, which may be extremely dominant during terminal guidance for low-cost devices. Therefore, development of new algorithms which may satisfy the needed accuracy levels at low cost during terminal guidance is a cornerstone in research on ballistic projectiles. For example, modern laser guided ballistic rockets are integrating IMU, GPS and laser guidance capability, offering high precision and all-weather attack capability (de Celis and Cadarso 2019; Zhang, Yang, Sun, Yang, Han, and Hu 2017).

Semi Active Laser Kits (SAL) have been developed to improve precision in guided rockets. SAL are currently applied in many engineering ambit, for example in determining rotational velocity of objects or in measuring slight movements of laser spots (Zeng, Zhu, and Chen 2016; Esper-Chaín, Escuela, Fariña, and Sendra 2015). One of the greatest advantages of this equipment is its high performance in terms of guidance, typically during the last phases of the trajectory, as compared to its low cost.

Sensor hybridisation methodologies and algorithms which aim at proposing effective and robust measures that allow for a high level of autonomy and precision at a low cost are a current need. In this sense, a promising methodology is what is known as Machine Learning (ML). It offers innumerable possibilities and revolutionary solutions of special interest for GNC applications, where its foray is still recent and shallow, but undoubtedly promising. Indeed, the use of ML methods for the estimation of parameters based on the dynamics of aerospace vehicles presents the advantage that once the algorithm is trained or calibrated, it is not necessary to know the physical-mathematical foundations that govern dynamics, but it is the algorithm that, for the input data, returns the information that can later be used within the GNC algorithm (Solano-López, de Celis, Fuentes, Cadarso, and Barea 2019), (Mohamed and Dongare 2018).

The aim of this paper is to improve the existing methods for terminal guidance applying an effective hybridization algorithm, which is based on a neural network. The objective is to obtain an accurate vector between rocket and target to be employed on a guidance, navigation, and control system from a combination of different sensors measures.

1.1 Contributions

The main contribution of this scientific research is the proposal of neural networks to hybridize GNSS / IMU and semi-active laser quadrant photo-detectors signals. The objective is to predict the line of sight, i.e., the vector linking the target and the rocket mass center, during terminal guidance, consequently improving

accuracy at the point of impact. It should be noted that the advantage of such a combined system over the GNSS / IMU one is the ability to avoid distortion and modify final impact angles.

The presented approach is based on two neural networks which predict the movement of the terminal line of sight. Inputs for neural networks are GNSS / IMU and semi-active laser quadrant photo-detectors signals. Line of sight is then integrated on a modified proportional navigation law and on a rotatory control technique. As controller, a robust double-input double-output controller is proposed, which can deal with the substantial coupling between the lateral and normal rocket nonlinear dynamics.

The utilization of a flight dynamics model reproducing a highly spinning rocket, which considers non-linearities in aerodynamic forces and moments, is proposed to build up a realistic simulation campaign. Simulation results exhibit the exactness and applicability of these algorithms under nondeterministic environment, launch and projectile conditions.

This paper is organized as follows: in Section II the system modeling is described in detail. Section III describes navigation, guidance, and control algorithms. Section IV exposes simulations results. Finally, discussion and conclusions are presented.

2 SYSTEM MODELING

This section focuses on the description of the plant, the non-linear flight mechanics model, actuation and sensor models, and hybridization used for navigation purposes.

2.1 Rocket Definition

The proposed guidance, navigation and control approach is applied to a 140 mm axis symmetric rotary rocket with wrap-around stabilizing fins as shown in Figure 1. Launch speed is supersonic and initial spin rate is approximately 150 Hz. The maneuvering mechanism consists of a roll-decoupled fuse attached to the tip of the rocket. The fuse is made up of four canard surfaces, decoupled 2 by 2, to generate control force modulus and argument in an orthogonal plane to the rocket section, and its associated moment (de Celis, Cadarso, and Sánchez 2017).

Figure 1: Rocket configuration.

Thrust, mass and aerodynamic characteristic parameter values for the rocket are shown in Tables 1 and 2. They are based on experimental measurements, fluid dynamics numerical simulations and wind tunnel verification. A cubic spline interpolation has been used to keep continuity and derivability on thrust and aerodynamic coefficients at intermediate points.

Table 1: Thrust and mass rocket parameters.

Parameter	Maximum thrust	Burn-out time	Initial mass	Propellant mass	I_{x0}	I_{y0}	X_{CG0}	Caliber
Value	29160.00 N	2.70 s	62.40 kg	21.00 kg	0.19 kgm^2	18.85 kgm^2	1.13 m	0.14 m

Time (s)	0	0.02	0.10	0.20	0.70	1.70	1.75	1.95	2	2.15	2.30	2.70
Thrust (kN)	0	25	22.5	23	24	28.5	29.1	15	10	5	2.5	0

2.2 Flight Dynamics Model

Before going into model details, three axes systems are defined to express forces and moments: body axes, earth axes and working axes. Body axes are defined by sub index b. x_b pointing forward and contained

Table 2: Aerodynamic rocket parameters.

M	$C_{D_0}(M)$	$C_{D_{\alpha^2}}(M)$	$C_{L_\alpha}(M)$	$C_{L_{\alpha^3}}(M)$	$C_{mf}(M)$	$C_{Nq}(M)$	$C_{M_\alpha}(M)$	$C_{M_{\alpha^3}}(M)$	$C_{M_q}(M)$	$C_{mm}(M)$	$C_{spin}(M)$	$C_{N\alpha_w}(M)$
0,00	0,27	10,74	8,01	19,82	-0,59	50,81	-35,58	-16,65	-225,73	3,02	-0,04	0,00
0,60	0,24	11,10	8,43	19,12	-0,70	57,43	-36,00	-20,39	-245,32	3,57	-0,04	0,43
0,80	0,23	11,40	8,79	18,49	-0,75	63,80	-36,51	-23,39	-264,85	3,84	-0,03	0,44
0,90	0,23	11,45	8,98	17,28	-0,78	67,93	-36,57	-18,48	-276,57	3,98	-0,03	0,45
1,00	0,41	15,12	8,93	44,05	-0,81	71,38	-35,99	15,39	-287,82	4,12	-0,03	0,45
1,10	0,48	15,09	8,99	43,00	-0,83	76,53	-35,54	19,12	-302,58	4,25	-0,03	0,45
1,50	0,41	13,99	8,10	41,97	-0,94	86,55	-27,05	26,25	-289,17	4,80	-0,03	0,40
2,00	0,35	13,02	7,28	41,27	-1,07	110,51	-17,62	24,77	-267,48	5,49	-0,02	0,35

in the plane of symmetry of the rocket, z_b perpendicular to x_b pointing down and contained in the plane of symmetry of the rocket, and y_b forming a clockwise trihedron. The origin of body axes is located at the center of mass of the rocket and they are severely coupled to the roll-decoupled fuse. Earth axes are defined by sub index e. x_e pointing north, z_e perpendicular to x_e and pointing nadir, and y_e forming a clockwise trihedron. Working axes are defined by sub index w. x_w pointing to the target, y_w perpendicular to x_w and pointing zenith, and z_w forming a clockwise trihedron. AZ_0 is the initial azimuth between x_e and x_w. Next, flight dynamics and actuation equations are introduced.

Total external forces and moments for the rocket are given in 1.

$$\left[\begin{array}{cc} \overrightarrow{F_{ext}} & , \quad \overrightarrow{M_{ext}} \end{array} \right] = \left[\begin{array}{cc} \overrightarrow{D} + \overrightarrow{L} + \overrightarrow{M} + \overrightarrow{P} + \overrightarrow{T} + \overrightarrow{W} + \overrightarrow{C} & , \quad \overrightarrow{O} + \overrightarrow{P_M} + \overrightarrow{M_M} + \overrightarrow{S} \end{array} \right], \tag{1}$$

where $\overrightarrow{D}$ is drag force, $\overrightarrow{L}$ is lift force, $\overrightarrow{M}$ is Magnus force, $\overrightarrow{P}$ is pitch damping force, $\overrightarrow{T}$ is thrust force, $\overrightarrow{W}$ is weight force, $\overrightarrow{C}$ is Coriolis force, $\overrightarrow{O}$ is overturn moment, $\overrightarrow{P_M}$ is pitch damping moment, $\overrightarrow{M_M}$ is Magnus moment and $\overrightarrow{S}$ is spin damping moment.

Rocket forces in working axes are described in 2 and 3. They include contributions from drag, lift, Magnus, pitch damping, thrust, weight and Coriolis forces:

$$\left[\begin{array}{cc} \overrightarrow{D} & , \quad \overrightarrow{L} \\ \overrightarrow{M} & , \quad \overrightarrow{P} \end{array} \right] = -\frac{\pi}{8} d^2 \rho \left[\begin{array}{cc} \left(C_{D_0}(M) + C_{D_{\alpha^2}}(M)\alpha^2\right) \|\overrightarrow{v_w}\| \overrightarrow{v_w} & , \quad \left(C_{L_\alpha}(M) \cdot \alpha + C_{L_{\alpha^3}}(M)\alpha^2\right) \left(\|\overrightarrow{v_w}\|^2 \overrightarrow{x_w} - (\overrightarrow{x_w} \cdot \overrightarrow{v_w}) \overrightarrow{v_w}\right) \\ d\frac{C_{mf}(M)}{I_x} \left(\overrightarrow{L_w} \cdot \overrightarrow{x_w}\right) (\overrightarrow{x_w} \times \overrightarrow{v_w}) & , \quad -d\frac{C_{Nq}(M)}{I_y} \|\overrightarrow{v_w}\|^2 \left(\overrightarrow{L_w} \times \overrightarrow{x_w}\right) \end{array} \right] \tag{2}$$

$$\left[\begin{array}{ccc} \overrightarrow{T} & , \quad \overrightarrow{W} & , \quad \overrightarrow{C} \end{array} \right] = \left[\begin{array}{ccc} T(t) \overrightarrow{x_w} & , \quad m\overrightarrow{g_w} & , \quad -2m\overrightarrow{\Omega} \times \overrightarrow{v_w} \end{array} \right], \tag{3}$$

where d is rocket caliber, ρ is air density, $C_{D_0}(M)$ is drag force linear coefficient, $C_{D_{\alpha^2}}(M)$ is drag force square coefficient, α is total angle of attack, $C_{L_\alpha}(M)$ is lift force linear coefficient, $C_{L_{\alpha^3}}(M)$ is lift force cubic coefficient, $C_{mf}(M)$ is Magnus force coefficient, $\overrightarrow{L_w}$ is rocket angular momentum in working axes, I_x *and* I_y are rocket inertia moments in body axes, $C_{Nq}(M)$ is pitch damping force coefficient, $\overrightarrow{x_w}$ is rocket nose pointing vector in working axes, $\overrightarrow{g_w}$ is gravity vector in working axes, $\overrightarrow{\Omega}$ is earth angular speed vector, and $\overrightarrow{v_w}$ is rocket velocity in working axes. Note that all these expressions are deeply nonlinear as aerodynamic linear, quadratic, and cubic coefficients depend on Mach number, which varies along the rocket flying performance.

Rocket moments, defined in 4, include overturning, pitch damping, Magnus, and spin damping moment:

$$\left[\begin{array}{cc} \overrightarrow{O} & , \quad \overrightarrow{P_M} \\ \overrightarrow{M_M} & , \quad \overrightarrow{S} \end{array} \right] = \frac{\pi}{8} d^3 \rho \left[\begin{array}{cc} \left(C_{M_\alpha}(M) + C_{M_{\alpha^3}}(M)\alpha^2\right) \|\overrightarrow{v_w}\|^2 \ (\overrightarrow{v_w} \times \overrightarrow{x_w}) & , \quad \frac{1}{I_y} C_{M_q}(M) \|\overrightarrow{v_w}\| \left(\overrightarrow{L_w} - \left(\overrightarrow{L_w} \cdot \overrightarrow{x_w}\right) \overrightarrow{x_w}\right) \\ -\frac{d}{I_x} C_{mm}(M) \left(\left(\overrightarrow{L_w} \cdot \overrightarrow{x_w}\right) ((\overrightarrow{v_w} \cdot \overrightarrow{x_w}) \overrightarrow{x_w}) - -\overrightarrow{v_w}\right) & , \quad \frac{d}{I_x} C_{spin}(M) \|\overrightarrow{v_w}\| \left(\overrightarrow{L_w} \cdot \overrightarrow{x_w}\right) \overrightarrow{x_w} \end{array} \right], \tag{4}$$

where $C_{M_\alpha}(M)$ is overturning moment linear coefficient, $C_{M_{\alpha^3}}(M)$ is overturning moment cubic coefficient, $C_{M_q}(M)$ is pitch damping moment coefficient, $C_{mm}(M)$ is Magnus moment coefficient and $C_{spin}(M)$ is spin damping moment coefficient. Non-linearities are once again considered.

Fuse mass is assumed to be negligible, which involves no reactions between fuse and aft part. Then, aft-fuse interactions can be expressed as an addition of external forces and moments, which are shown in equation 5. This simplification is obtained from Euler equations, $\overrightarrow{F_{ext}} = \frac{dm\overrightarrow{v_b}}{dt} + \overrightarrow{\omega_b} \times m\overrightarrow{v_b}$ on where gyroscopic contributions of the aft part are moved to the left part of the expression and operated separately.

$$\begin{bmatrix} \overrightarrow{M_r} & , & \overrightarrow{M_{Mr}} \\ & \overrightarrow{G_r} & \end{bmatrix} = \begin{bmatrix} -\frac{\pi}{8} d^3 \rho \left[\frac{C_{mf}(M)}{I_x} \left(\overrightarrow{L_b} \cdot \overrightarrow{x_b} \right) (\overrightarrow{x_b} \times \overrightarrow{v_b}) \quad , \quad \frac{d}{I_x} C_{mm}(M) \left(\left(\overrightarrow{L_b} \cdot \overrightarrow{x_b} \right) ((\overrightarrow{v_b} \cdot \overrightarrow{x_b}) \overrightarrow{x_b}) - \overrightarrow{v_b} \right) \right] \\ -\bar{\bar{I}} \frac{d}{dt} \left(\overrightarrow{\omega_b} + p_r \overrightarrow{x_b} \right) + \overrightarrow{\omega_b} \times \bar{\bar{I}} \left(\overrightarrow{\omega_b} + p_r \overrightarrow{x_b} \right) \end{bmatrix} \tag{5}$$

$\overrightarrow{M_r}$ is Magnus force of the rotating part of the rocket, $\overrightarrow{M_{Mr}}$ is Magnus moment of the rotating part of the rocket, $\overrightarrow{G_r}$ is gyroscopic moment of the rotating part of the rocket, p, q *and* r are angular speed components of the rocket, p_r is angular speed of the rotating part of the rocket, $\overrightarrow{L_b}$ is rocket angular momentum in body axes, $\overrightarrow{v_b}$ is rocket velocity in body axes and $\overrightarrow{x_b}$ is rocket nose pointing vector in body axes.

Given the force and moment models above, the equations of motion for the rocket are formulated using a Newton-Euler approach, which is shown in 6. Note that the inertial, flat-Earth coordinate system (denoted by frame e) and the body-fixed coordinate system b are related by Euler roll (ϕ), pitch (θ), and yaw (ψ) angles.

$$\left[\overrightarrow{CF} + \overrightarrow{F_{ext}} + \overrightarrow{M_r} \quad , \quad \overrightarrow{CM} + \overrightarrow{M_{ext}} + \overrightarrow{M_{Mr}} + \overrightarrow{G_r} \right] = \left[\frac{dm\overrightarrow{v_b}}{dt} + \overrightarrow{\omega_b} \times m\overrightarrow{v_b} \quad , \quad \frac{d\overrightarrow{L_b}}{dt} + \overrightarrow{\omega_b} \times \overrightarrow{L_b} \right] \tag{6}$$

Note that the control force ($\overrightarrow{CF}$) and moment ($\overrightarrow{CM}$) for each fin are given in equation 7:

$$\begin{bmatrix} \overrightarrow{CF} \\ \overrightarrow{CM} \end{bmatrix} = \Sigma_{i=1}^{i=4} \begin{bmatrix} \frac{1}{8} sign(\alpha_{eff_i}) d^2 \rho \pi \| \overrightarrow{v_{eff_{x_i}}} \|^2 (C_{N\alpha_w}(M) cos(\alpha_{eff_i}) + \frac{2}{d^2\pi} S_{exp} sin^2(\alpha_{eff_i})) (\overrightarrow{u_{FN_i}} cos\delta_i - \overrightarrow{x_b} sin\delta_i) \\ (d_{ax}(M)\overrightarrow{x_b} + d_{lat}\overrightarrow{u_{b_i}}) \times \frac{1}{8} sign(\alpha_{eff_i}) d^2 \rho \pi \| \overrightarrow{v_{eff_{x_i}}} \|^2 (C_{N\alpha_w}(M) cos(\alpha_{eff_i}) + \frac{2}{d^2\pi} S_{exp} sin^2(\alpha_{eff_i})) (\overrightarrow{u_{FN_i}} cos\delta_i - \overrightarrow{x_b} sin\delta_i), \end{bmatrix} \tag{7}$$

where $C_{N\alpha_w}(M)$ is the aerodynamic coefficient of the normal force for a fin, S_{exp} is the characteristic surface of the airfoil, α_{eff_i} is the effective angle of attack (de Celis and Cadarso 2018), $d_{ax}(M)$ is the longitudinal distance, parallel to x_b, of airfoil center of pressure (CP) to rocket center of mass (CG), which depends on the Mach number (M) and introduces another source of non-linearity. d_{lat} is the lateral distance, which is orthogonal to x_b and parallel to u_{b_i} for each fin, from airfoil center of pressure to rocket center of mass. It is assumed to be constant in this model.

2.3 Sensors

Two different sensor sets are introduced. A GNSS/IMU system and a semi-active laser quadrant photo detector.

The GNSS/IMU system is modeled to permit good performance for intermediate trajectories. A bias and a random noise are added to the calculated position and attitude. Note that these hybridized systems' accuracy is on the order of magnitude of 1 m for position and 0.1 degrees for attitude. Equation 8 shows the vector between rocket and target (line of sight $\overrightarrow{X_{p_{wGNSS/IMU}}}$):

$$\overrightarrow{X_{p_{wGNSS/IMU}}} = \left[x_{w_{T_{GNSS/IMU}}} - x_{w_{R_{GNSS/IMU}}} \quad , \quad y_{w_{T_{GNSS/IMU}}} - y_{w_{R_{GNSS/IMU}}} \quad , \quad z_{w_{T_{GNSS/IMU}}} - z_{w_{R_{GNSS/IMU}}} \right], \tag{8}$$

where $[x_{w_{T_{GNSS/IMU}}}, y_{w_{T_{GNSS/IMU}}}, z_{w_{T_{GNSS/IMU}}}]$ is the position of the target in working axes, and $[x_{w_{R_{GNSS/IMU}}}, y_{w_{R_{GNSS/IMU}}}, z_{w_{R_{GNSS/IMU}}}]$ is the position of rocket center of gravity at each instant in working axes, as measured by the GNSS/IMU system.

In terminal flight guidance, 1 m errors in rocket and target positioning induce huge angular errors in the line of sight vector. An accurate terminal guidance sensor such as a semi-active laser quadrant photo detector may be used to mitigate this drawback (de Celis and Cadarso 2019). To calculate laser footprint centroid coordinates, the electric intensities generated in the photo diodes (I_1, I_2, I_3 and I_4) are used, which depend on the illuminated area. These coordinates can be calculated as $[ln\frac{I_4}{I_2}, ln\frac{I_1}{I_3}]$, and from them the measured radial distance, r_{quad}, can be obtained. However, real coordinates differ from the previous ones, although the transformation is conformal (de Celis and Cadarso 2019). Relationship between r_{quad} and real radial distance, r_c, i.e., $r_c = f(r_{quad})$, is shown in Table 3. These radial measurements are interpolated using cubic splines to calculate real spot center coordinates (de Celis and Cadarso 2019):

Table 3: Interpolation between measured radial distance, r_{quad}, and real radial distance, r_c.

$r_{quad} = \sqrt{ln\frac{I_4}{I_2}^2 + ln\frac{I_1}{I_3}^2}$	0.48	0.99	1.50	2.01	2.67	3.68	5.88
r_c	0.1	0.2	0.3	0.4	0.5	0.6	0.7

$$\overrightarrow{X_{p_b}} = \frac{R_{quad} r_c}{r_{quad}} \left(d_{pCG}^2 + \left(ln\frac{I_4}{I_2} \right)^2 + \left(ln\frac{I_3}{I_1} \right)^2 \right)^{-\frac{1}{2}} \cdot \left(d_{pCG}\overrightarrow{x_b} + \frac{R_{quad} r_c}{r_{quad}} ln\frac{I_4}{I_2}\overrightarrow{y_b} + \frac{R_{quad} r_c}{r_{quad}} ln\frac{I_3}{I_1}\overrightarrow{z_b} \right) \quad (9)$$

where R_{quad} is the physical radius of the quadrant detector. Therefore, the line of sight vector, expressed in body axes, shall respond to the expression in 9, where d_{pCG} is the distance from the quadrant detector to the center of mass of the rocket. The combination of these sensors may provide an accurate definition of the line of sight vector if their signals are correctly hybridized. Next navigation, guidance and control algorithms are introduced. At their core, neural networks are introduced to fuse semi-active laser kit and GNSS/IMU sensor signals to increase projectile accuracy.

3 NAVIGATION, GUIDANCE AND CONTROL

This section describes the proposed navigation, guidance, and control algorithms.

3.1 Navigation

Navigation process refers to the determination, during the whole trajectory, of the rocket and target positions and rocket attitude. The aim is to obtain the line of sight between them, which can be calculated in earth axes by subtracting rocket position, determined by GNSS/IMU sensors, from target position, but as it was previously explained, this method induces enormous angular errors during final phases of flight. Semi-active laser quadrant detector may provide an accurate line of sight in body axes during last stages of flight. Line of sight vector, both in working and earth axes, ($\overrightarrow{X_{p_w}}$) and ($\overrightarrow{X_{p_e}}$) respectively, can be obtained from hybridized signals of GNSS/IMU and semi-active laser kit sensors.

3.1.1 Hybridization Algorithm

The hybridization process is based on Neural Networks (NN). The aim is to recover a high accuracy on the line of sight determination process by combining the measurements from the quadrant detector, the IMU/GNSS and the potential offered by NNs.

Among the many applications that ML offers to classic and modern GNC problems (see (Yu, Zhang, and Gu 2004), (Jankovic, Paul, and Kirchner 2016), (Mohamed and Dongare 2018), (Villa, Taipalmaa, Gerasimenko, Pyattaev, Ukonaho, Zhang, Raitoharju, Passalis, Perttula, Aaltonen, et al. 2020)), the main advantage of NNs against other approximations lies in their possibility to learn flight dynamics equations, which enables flight prediction without the need of knowing the physical problem (Yadav, Yadav, and

Kumar 2015). This feature makes possible to replicate the determination process of a line of sight from sensor data. The use of NN to solve the evolution of non-linear equations has been proved before (Yadav, Yadav, and Kumar 2015), even if they feature uncertainty.

Two neural networks are utilized to estimate x_c and y_c, which are the real spot center coordinates. They both are employed in the proposed hybridization approach. They feature two-layers with one hundred standard sigmoid hidden neurons and a linear output neuron. The choice of the number and shape of neurons (e.g., sigmoid activation function), and the selected amount of training and validation data are based on the literature review (specially from (Yadav, Yadav, and Kumar 2015)) and on a hyperparametric study. As a result, the approximate numbers of 100 and 50 were obtained to be significant as the number of neurons. Other experiments using 50 neurons and 75 neurons have been performed and results are significantly worse as compared to the provided results (more than 10%). Further research will be performed to precisely determine the optimal working point. But, it is not the objective of this paper to formalize this statement.

The input vector is composed of 3 components, the signals from the GNSS/IMU and SAL, and a binary signal which is 1 if SAL receives data, and 0 otherwise. The target is the line of sight. Consequently, NN are trained replicating the flight dynamics. Table 4 shows an example of the available $3 \cdot 10^8$ rows of data, which are obtained from 24000 simulations, where flight mechanics initial and contour conditions are varied to minimize bias and avoid overfitting. The architecture of neural networks are showed in Figure 2.

Levenberg-Marquardt backpropagation algorithm (Kanzow, Yamashita, and Fukushima 2005) is used to train the network with a 70% of the available data. And a representative amount of sensor data and its corresponding line of sight are left aside for validation purposes. In this case, a 15% of the available data.

The performance of the training algorithm can be quantified by means of the Mean Squared Error (MSE) and the Regression (R) parameter values. The MSE is the average squared difference between outputs and targets. Lower values are better, and zero means no error. R values measure the correlation between outputs and targets. An R value of 1 means a close relationship, and 0 a random relationship. Other indicators (such as Mean average error, MAE) can also be used to monitor and validate the training while overfitting is avoided. The training process is considered complete when the MSE stops improving.

After 1000 iterations and a validation process, a MSE value of $3.1 \cdot 10^{-5}$ for x_c, $2.1 \cdot 10^{-5}$ for y_c, and a parameter for regression of 0.98 for x_c, and 0.99 for y_c are obtained. As showed in the numerical simulations, these results are good enough for the studied application. In addition, the trained NN is tested with the independent data (15% of the collected data), producing similar MSE and R values.

Table 4: Neural Network Input and Target values.

GNSS/IMU Inputs		SAL Inputs		Target	
x_c	y_c	x_c	y_c	x_c	y_c
0.012	0.006	0.012	0.006	0.025	0.002
0.011	0.006	0.011	0.006	0.024	0.001
...	...	...	...	...	...

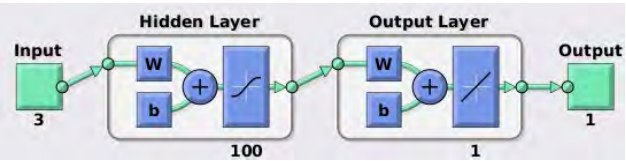

Figure 2: Neural Network scheme.

As an example, for a nominal shot (de Celis, Cadarso, and Sánchez 2017), a typical error on GNSS/IMU sensors of 1 m on each of the three position components, and a random white noise for the quadrant detector of 0.001 on each of the two measurements, the results for the proposed hybridizing algorithm are shown

in Figure 3, where x and y coordinates for the line of sight are shown. Note that z coordinate is known as it is measured from the center of mass of the rocket. As it is shown in the figure, the GNSS/IMU measurements (black line) degrade during the last stages of flight, while the hybridized solution (red line) keeps fidelity to the real line of sight (blue line) during the whole trajectory. Here, the physical radius of quadrant detector, R_{quad}, has been set to 8 mm.

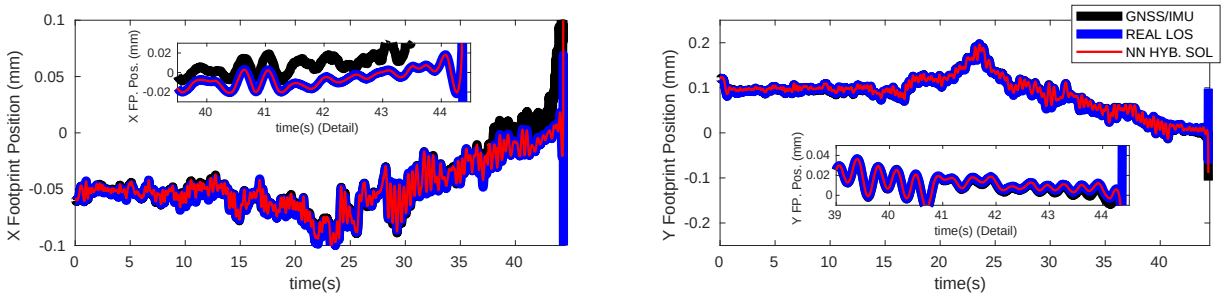

Figure 3: Results for the hybridization algorithm: x and y coordinates for the line of sight.

3.2 Guidance Law

Guidance is provided in two phases. The first one consists of a constant angle glide trajectory, while the second one consists of a modified proportional law.

3.2.1 Constant Angle Glide Trajectory

The proposed law (equation 10) is elected to maximize projectile range. It aligns longitudinal rocket axis (x_b) with a vertical flight plane, perpendicular to ground, parallel to the line joining the rocket center of mass and the target and containing the rocket center of mass. Vector $\overrightarrow{X_{p_w}} = [x_{p_w}, y_{p_w}, z_{p_w}]$, which represents the line of sight, is expressed in working axes by its three components. Vector $\overrightarrow{x_{b_w}} = [x_{b1_w}, x_{b2_w}, x_{b3_w}]$, which represents x_b in working axes, is again expressed by its three components. The first component of equation 10 represents the lateral correction (ψ_{dem}) and the second component represents correction in the vertical plane (θ_{dem}) with respect to a constant glide angle trajectory given by C_1 (de Celis, Cadarso, and Sánchez 2017). This constant angle glide guidance is only activated when the rocket is after apogee, which is determined by the pitch angle (θ), and flight time is long enough to thrust be off.

$$\begin{bmatrix} \psi_{dem} & , & \theta_{dem} \end{bmatrix} = \begin{cases} \begin{bmatrix} (atan\frac{z_{p_w}}{x_{p_w}} - atan\frac{x_{b3_w}}{x_{b1_w}}) & , & C_1 \end{bmatrix} & \text{if } t > 5 \text{ and } \theta \leq 0 \\ \begin{bmatrix} 0 & , & 0 \end{bmatrix} & \text{else} \end{cases} \tag{10}$$

3.2.2 Modified Proportional Law

The terminal phase consists of a modified proportional law governed by equation 11. Equation 12 estimates time to impact, t_{go}. Guidance is only activated when the vertical component of line of sight vector is higher than a given constant (C_2) (de Celis, Cadarso, and Sánchez 2017).

$$\begin{bmatrix} \psi_{dem} & , & \theta_{dem} \end{bmatrix} = \begin{cases} \frac{\overrightarrow{X_{p_w}} - \overrightarrow{v_w} t_{go}}{t_{go}^2} \cdot \begin{bmatrix} \overrightarrow{k_w} & , & -\overrightarrow{i_w} \end{bmatrix} & \text{if } atan\frac{z_{p_e}}{\sqrt{x_{p_e}^2 + y_{p_e}^2}} \leq C_2 \\ \begin{bmatrix} 0 & , & 0 \end{bmatrix} & \text{else} \end{cases} \tag{11}$$

$$t_{go} = max \begin{bmatrix} \frac{1}{g}\left(\overrightarrow{v_w} \cdot \overrightarrow{j_w} + \sqrt{(\overrightarrow{v_w} \cdot \overrightarrow{j_w})^2 + 2gy_{p_w}}\right), & \frac{1}{g}\left(\overrightarrow{v_w} \cdot \overrightarrow{j_w} - \sqrt{(\overrightarrow{v_w} \cdot \overrightarrow{j_w})^2 + 2gy_{p_w}}\right) \end{bmatrix} \tag{12}$$

where $\overrightarrow{v_w}$ is rocket speed vector expressed in working axes and g is the gravity constant.

3.3 Control System

The control law introduced in (de Celis and Cadarso 2018) is integrated in the current system. Two control parameters are introduced in the actuation system: the angle and the modulus for the rotating force. Control is processed by a double loop feedback system. The inner loop is only used as a system of stability augmentation. The control angle (ϕ_c) and modulus (τ_c) of the rotating force are defined in equation 13, taking pitch (θ_{dem}) and yaw (ψ_{dem}) errors as inputs. $L1$ and $L2$ are experimental gains, K_i, K_d and K_p are the integral, derivative, and proportional constants of the controller, and K_{mod} is a constant to adjust force module. In (de Celis, Cadarso, and Sánchez 2017), the process to determine these constant values, which are shown in Table 5, is explained.

$$\begin{bmatrix} \phi_c \\ \tau_c \end{bmatrix} = \begin{bmatrix} K_p\,(E1-E2)+K_i\int(E1-E2)\,dt+K_d\frac{d}{dt}(E1-E2)+E1 \\ K_{mod}\sqrt{(\theta_{dem}-L_1\theta)^2+(L_2(\psi_{dem}-L_1\psi))^2} \end{bmatrix} \text{ where } \begin{cases} E1 = atan\frac{\theta_{dem}-L_1\theta}{L_2(\psi_{dem}-L_1\psi)} \\ E2 = atan\frac{acc_{zb}}{acc_{yb}} \end{cases} \tag{13}$$

Table 5: Values for the constants on each flight phase.

Parameter	C_1	C_2	K_i	K_p	K_d	K_{mod}	L_1	L_2
Value for phase 1	-7.5 deg	-21 deg	0	0.5	0	0.08	0.01	100
Value for phase 2	-7.5 deg	-21 deg	1	0.25	0.05	0.08	0.01	1

$[acc_{xb}, acc_{yb}, acc_{zb}]$ is the acceleration of the rocket in body axes and $[\phi, \theta, \psi]$ are the Euler angles as introduced before. Roughly speaking, the controller calculates the needed pointing angle of the aerodynamic force calculating the arctangent of the quotient of the pitch and yaw error. This gives an angle at which the aerodynamic force, in the $y_b - z_b$ plane, must point to reach the target. However, the gyroscopic effect due to the spinning part of the rocket makes the response difficult to govern, i.e., pointing the control force upwards will not make the rocket to respond upwards. Therefore, we also need to measure the acceleration of the rocket, without accounting for gravity, and make the difference between the angle of the projection of the aerodynamic force in the $y_b - z_b$ plane with y_b and ϕ_c zero (de Celis, Cadarso, and Sánchez 2017).

These control parameters are translated into fin deflections, i.e., $\delta_1, \delta_2, \delta_3$ and δ_4, which are managed by two actuators, by means of equations 14.

$$\begin{bmatrix} \delta_1 & , & \delta_2 & , & \delta_3 & , & \delta_4 \end{bmatrix} = \tau_c \begin{bmatrix} sin\phi_c & , & cos\phi_c & , & sin\phi_c & , & cos\phi_c \end{bmatrix} \tag{14}$$

4 NUMERICAL SIMULATIONS

The previous nonlinear equations of motion are integrated forward in time using a fixed time step Runge-Kutta scheme of fourth order to obtain a single flight trajectory. The validation of this modelling and solving approach for ballistic flights is shown in (de Celis, Cadarso, and Sánchez 2017). To demonstrate the accuracy of the results provided by the novel approach presented here, which is based on neural networks, they are compared to the results obtained in (de Celis, Cadarso, and Sánchez 2017) and (de Celis and Cadarso 2018). The approach in (de Celis, Cadarso, and Sánchez 2017) features a control based on a GNSS/IMU system while the one in (de Celis and Cadarso 2018) features a Kalman based hybridization of a GNSS/IMU system and a semi-active laser quadrant photo-detector. MATLAB/Simulink R2020a on a desktop computer with a processor of 2.8 GHz and 8 GB RAM is employed in the simulations.

4.1 Ballistic Trajectories

To test the algorithms developed, three nominal trajectories will be employed. They differ in their initial pitch angle: 20°, 30° and 45°. Impact points are at 18790 m, 23007 m, and 26979 m, respectively. Initial lateral correction is set to compensate Coriolis and gyroscopic forces: 0.15°, 0.19° and 0.31°, respectively.

4.2 Monte Carlo Simulations

Monte Carlo analysis is conducted to determine closed-loop performance across a full spectrum of uncertainty at initial conditions, sensor data acquisition, atmospheric conditions, and thrust properties. Uncertainty model details for sensors are defined in previous sections and the rest are shown in Table 6. A set of 2000 shots is performed for each of the following combinations: ballistic shots, Kalman hybridization guidance, neural network hybridization guidance and ideal shots. Then, a total of 24000 simulations are performed at the end of simulation campaign. Note that this simulation campaign is different from the training one.

Table 6: Monte Carlo simulation parameters.

Parameter (deg)	Initial ϕ	Initial Pitch	Wind Speed	Wind Direction	Thrust	Initial azimuth
Mean	0°	Nom.	10 m/s	0°	T(t)	Nom.
Standard Deviation	20°	0.01°	5 m/s	20°	10 N	0.01°

4.3 Discussion

Results for ballistic trajectories and comparisons between different approaches are shown in Figure 4. It is composed of four columns and three rows of sub-figures. Each row features a different initial pitch angle. The first column of sub-figures compares ballistic flights against Kalman hybridization assisted flights, the second one compares Kalman hybridization against Neural Network hybridisation, the third one Neural Network hybridization against ideal controller, and the last one ballistic flights against Neural Network hybridization assisted flights. Note that, even with an ideal controller, which features perfect information on the line of sight, there are still errors associated to the aerodynamic response of the rocket. As a general remark, controlled flights exhibit tighter impact groupings, getting similar results for both hybridizations and ideal controller. Note that improvements or reductions on the CEP of a 95% are obtained. The circular error probable (CEP) for each of the initial pitch angles and ballistic and controlled flights is shown in Table 7.

Table 7: Circular Error Probable for different algorithms.

Initial Pitch (deg)	Ballistic (m)	Kalman Hyb. Control (m)	Neural Network Hyb. Control (m)	Ideal Control (m)
20	169.34	1.28	1.29	1.18
30	239.37	1.18	1.17	1.06
45	281.59	0.91	0.93	0.83

5 CONCLUSIONS

A novel approach, which is based on an innovative hybridization between GNSS/IMU and semi-active laser quadrant photo-detectors, has been developed. Small errors of 1 m in GNSS/IMU systems may induce significant errors in line of sight vector calculation. Note that when distance to target is small, these errors may result in high angular errors in line of sight. The proposed approach can improve the precision of line of sight determination during the terminal guidance, therefore ameliorating the precision on impact point.

A two-phase guidance algorithm and a novel control technique for high-rate spinning rockets are proposed. The guidance algorithm is based on a constant angle glide and on a modified proportional law while the control algorithm is based on a simple but effective and robust double-input double-output controller. Several algorithms are proposed for fusing signals of different sensors in the terminal trajectory. The novel proposed approach shows that levels of accuracy can be improved or matched as compared against other methodologies.

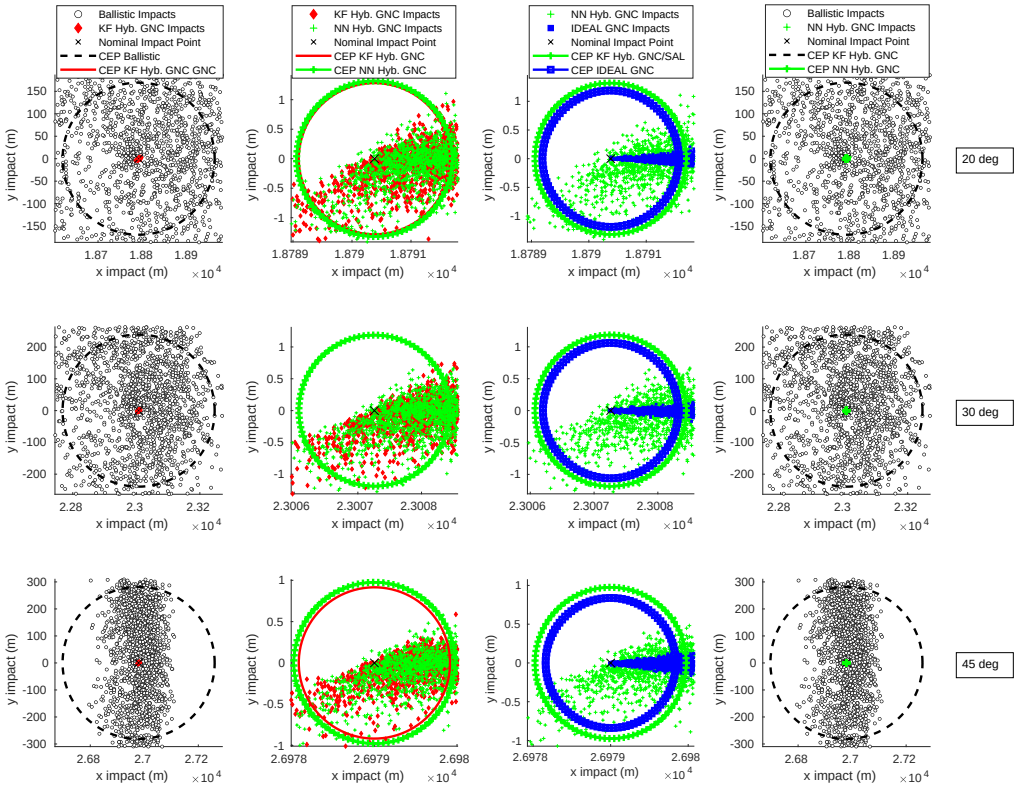

Figure 4: Detailed shots for different algorithms.

ACKNOWLEDGMENT

This research was supported by Project Grant F663 - AAGNCS by the "Consejería de Ciencia, Universidades e Innovación, Comunidad de Madrid" and "Universidad Rey Juan Carlos". The authors would like to thank Lt.C. Jesús Sánchez (NMT) of the INTA for the solid modeling of the concept.

REFERENCES

Bryne, T. H., J. M. Hansen, R. H. Rogne, N. Sokolova, T. I. Fossen, and T. A. Johansen. 2017. "Nonlinear observers for integrated INS\/GNSS navigation: implementation aspects". *IEEE Control Systems Magazine* 37(3):59–86.

Creagh, M. A., and D. J. Mee. 2010. "Attitude guidance for spinning vehicles with independent pitch and yaw control". *Journal of guidance, control, and dynamics* 33(3):915–922.

de Celis, R., and L. Cadarso. 2018. "GNSS/IMU laser quadrant detector hybridization techniques for artillery rocket guidance". *Nonlinear Dynamics* 91(4):2683–2698.

de Celis, R., and L. Cadarso. 2019. "Spot-Centroid Determination Algorithms in Semiactive Laser Photodiodes for Artillery Applications". *Journal of Sensors* 2019.

de Celis, R., L. Cadarso, and J. Sánchez. 2017. "Guidance and control for high dynamic rotating artillery rockets". *Aerospace Science and Technology* 64:204–212.

Esper-Chaín, R., A. M. Escuela, D. Fariña, and J. R. Sendra. 2015. "Configurable quadrant photodetector: an improved position sensitive device". *IEEE Sensors Journal* 16(1):109–119.

Hamilton, R. 1995. "Precision guided munitions and the new era of warfare". *Air Power Studies Centre, Royal Australian Air. DOI: http://fas. org/man/dod-101/sys/smart/docs/paper53. htm*.

Jankovic, M., J. Paul, and F. Kirchner. 2016. "GNC architecture for autonomous robotic capture of a non-cooperative target: preliminary concept design". *Advances in Space Research* 57(8):1715–1736.

Kanzow, C., N. Yamashita, and M. Fukushima. 2005. "Withdrawn: Levenberg–marquardt methods with strong local convergence properties for solving nonlinear equations with convex constraints". *Journal of Computational and Applied Mathematics* 173(2):321–343.

Lechevin, N., and C. A. Rabbath. 2012. "Robust discrete-time proportional-derivative navigation guidance". *Journal of guidance, control, and dynamics* 35(3):1007–1013.

Lee, H.-I., B.-C. Sun, M.-J. Tahk, and H. Lee. 2001. "Control design of spinning rockets based on co-evolutionary optimization". *Control Engineering Practice* 9(2):149–157.

Mohamed, M., and V. Dongare. 2018. "Aircraft neural modeling and parameter estimation using neural partial differentiation". *Aircraft Engineering and Aerospace Technology* 90(5):764–778.

Nesline, F. W., and P. Zarchan. 1985. "Line-of-sight reconstruction for faster homing guidance". *Journal of Guidance, Control, and Dynamics* 8(1):3–8.

Nguyen, N. V., M. Tyan, and J.-W. Lee. 2016. "Efficient Framework for Missile Design and 6DoF Simulation using Multi-fidelity Analysis and Data Fusion". In *17th AIAA/ISSMO Multidisciplinary Analysis and Optimization Conference*. June 13th-17th, Washington, D.C., U.S.A., 3365.

Schmidt, G. T., and R. E. Phillips. 2011. "INS/GPS integration architecture performance comparisons". *NATO RTO lecture series, low-cost navigation sensors and integration technology RTO-EN-SET-116*.

Solano-López, P., R. de Celis, M. Fuentes, L. Cadarso, and A. Barea. 2019. "Strategies for high performance GNSS/IMU Guidance, Navigation and Control of Rocketry". In *8th European Conference for Aeronautics and Space Sciences*. July 1st-3rd, Madrid, Spain.

Theodoulis, S., V. Gassmann, P. Wernert, L. Dritsas, I. Kitsios, and A. Tzes. 2013. "Guidance and control design for a class of spin-stabilized fin-controlled projectiles". *Journal of Guidance, Control, and Dynamics* 36(2):517–531.

Villa, J., J. Taipalmaa, M. Gerasimenko, A. Pyattaev, M. Ukonaho, H. Zhang, J. Raitoharju, N. Passalis, A. Perttula, J. Aaltonen et al. 2020. "aColor: Mechatronics, Machine Learning, and Communications in an Unmanned Surface Vehicle". In *Proceedings of 8th Transport Research Arena TRA 2020*. April 27th-30th, Helsinki, Finland.

Waltz, E. L., and D. M. Buede. 1986. "Data fusion and decision support for command and control". *IEEE Transactions on Systems, Man, and Cybernetics* 16(6):865–879.

Wang, X., J. Wang, and G. Gao. 2015. "Partial integrated missile guidance and control with state observer". *Nonlinear Dynamics* 79(4):2497–2514.

Yadav, N., A. Yadav, and M. Kumar. 2015. *An introduction to neural network methods for differential equations*. 1st ed. Dordrecht, Netherlands: Springer.

Yu, J.-Y., Y.-A. Zhang, and W.-J. Gu. 2004. "An approach to integrated guidance/autopilot design for missiles based on terminal sliding mode control". In *Proceedings of 2004 International Conference on Machine Learning and Cybernetics (IEEE Cat. No. 04EX826)*, edited by IEEE, Volume 1. New York, U.S.A: IEEE.

Zeng, X., Z. Zhu, and Y. Chen. 2016. "Remote evaluation of rotational velocity using a quadrant photo-detector and a DSC algorithm". *Sensors* 16(5):587.

Zhang, X., Z. Yang, T. Sun, H. Yang, K. Han, and B. Hu. 2017. "Optical system design with common aperture for mid-infrared and laser composite guidance". In *Second International Conference on Photonics and Optical Engineering*, Volume 10256, 102560S. International Society for Optics and Photonics.

Zhang, Y., M. Sun, and Z. Chen. 2012. "Finite-time convergent guidance law with impact angle constraint based on sliding-mode control". *Nonlinear Dynamics* 70(1):619–625.

Zhao, J., and R. Zhou. 2015. "Unified approach to cooperative guidance laws against stationary and maneuvering targets". *Nonlinear Dynamics* 81(4):1635–1647.

AUTHOR BIOGRAPHIES

RAUL DE CELIS is an assistant professor in aerospace area at Rey Juan Carlos University. He received his Ph.D. degree from Universidad Rey Juan Carlos in December 2017. His research interests are model development of aeronautic systems and navigation and control for aerial platforms. His email address is raul.decelis@urjc.es.

PABLO SOLANO LÓPEZ is an assistant professor in aerospace area at Rey Juan Carlos University. He received a Double MSc. degree in Aerospace Engineering from the Universidad Politécnica de Madrid, Spain and from the Institut Supérieur de l'Aéronautique et de l'Espace, France. His research interests revolve around numerical methods to solve complex non-linear problems and machine learning. His email address is pablo.solano@urjc.es.

LUIS CADARSO is an associate professor in aerospace area at Rey Juan Carlos University. He received the Ph.D. degree in Aerospace Engineering from the Technical University of Madrid, Spain. His research interests include operations research , navigation, and control for aerial platforms. His email address is luis.cadarso@urjc.es.